



Mesoporous Sn(IV) doping MCM-41 supported Pd nanoparticles for enhanced selective catalytic oxidation of 1,2-propanediol to pyruvic acid

Yonghai Feng^{a,*}, Wanli Li^{a,1}, Minjia Meng^b, Hengbo Yin^b, Jianli Mi^{a,*}

^a Institute for Advanced Materials, School of Materials Science and Engineering, Jiangsu University, Zhenjiang, 212013, China

^b School of Chemistry and Chemical Engineering, Jiangsu University, Zhenjiang, 212013, China

ARTICLE INFO

Keywords:

Selective catalytic oxidation
1,2-Propanediol
Pyruvic acid
Sn(IV) doping
Mesoporous structure

ABSTRACT

The conversion of biomass derivative 1,2-propanediol (PDO) to value-added chemicals by selective catalytic oxidation is of great research interest. Herein, we provide an alternative and effective strategy for selectively catalyzing the PDO oxidation to pyruvic acid using Sn(IV) doping MCM-41 (SnM) supported Pd nanoparticles (2%Pd/SnM) as catalyst, in which the SnM with the Si/Sn ratios ranging from 6 to 50 are prepared by direct hydrothermal synthesis (DHS) method and the Pd nanoparticles are in situ reduced on the SnM surfaces. When the Si/Sn ratios are above 12, decreasing the Si/Sn ratio favors the incorporation of more Sn(IV) species into the framework, the formation of smaller Pd nanoparticles with higher distribution and the increment of basicity, contributing to the significant enhancement in the selective oxidation of PDO to pyruvic acid, but if the ratio is further reduced to 6, larger Pd nanoparticles are formed in the 2%Pd/SnM6 with less ordered mesostructure due to excess Sn(IV) resulting in the formation of SnO₂ crystallites, displaying much lower catalytic activity than the 2%Pd/SnM12. The Sn(IV) species incorporated into MCM-41 can be used as effective promoter for enhancing the selective oxidation of PDO to pyruvic acid over the Pd/SnM catalyst.

1. Introduction

Facing great challenges of increasing energy consumption, expanding commodity demands, and environmental concerns, the utilization of renewable biomass to replace fossil feedstock for producing fuels, commodity chemicals, and polymeric materials has attracted much attention. Owing to the large surplus of glycerol formed as a by-product during the production of biodiesel, research efforts are made to use the glycerol as feedstock for the production of other valuable chemicals in order to enhance the competitiveness of the biodiesel industry [1]. One promising conversion of glycerol is to 1,2-propanediol (PDO) via hydrogenolysis, which has been commercialized by ADM and BASF [2]. The PDO is mainly used as an organic solvent or a starting material of unsaturated polyester resin, of which however the consumption is limited because a large amount of PDO is increasingly produced due to the scaling-up co-production of dimethyl carbonate and PDO by the transesterification method [3]. Thus, the development of PDO as a renewable feedstock molecule to produce more important industrial chemicals has received increasing interest.

The PDO has vicinal primary and secondary alcohol groups. It is attractive to transform it through selective oxidation pathways to lactic

acid by oxidation of the primary hydroxyl group, or to pyruvic acid by oxidation of the primary and secondary hydroxyl groups [4]. Many researches focus on the selective oxidation of PDO to lactic acid by various supported mono-/bi-metallic noble metal catalysts because of its importance in sustainable production of polymers, fibers, and solvents [4–17], while few to the pyruvic acid [4,18,19]. Owing to the important uses in health supplement, and as precursors for chemicals, pharmaceuticals and agrochemicals, the recent commercial demand of pyruvic acid is ever rising [20]. In spite of its expanding applications, the major production of pyruvic acid is through the traditional dehydrative decarboxylation of tartaric acid route, which however consumes a large amount of KHSO₄ and energy but with relatively low PA yield (50–55%) [19,21]. Finding renewable alternative pathways to produce PA under mild conditions is more desirable. Based on the merit of the renewability of PDO and the environmental friendliness of catalytic oxidation, it will be an alternative and resource-efficient way to produce pyruvic acid by the selective catalytic oxidation of PDO.

The catalytic oxidation of PDO to pyruvic acid is generally carried out under mild reaction conditions using heavy metals (eg. Pb, Bi, Te, or Sn) promoted noble metals (eg. Pt or Pd) as catalysts, which are prepared by impregnation of the heavy metal precursors on the

* Corresponding authors at: Institute for Advanced Materials, School of Materials Science and Engineering, Jiangsu University, Zhenjiang, 212013, China.

E-mail addresses: fengyonghai@ujs.edu.cn (Y. Feng), jlmi@ujs.edu.cn (J. Mi).

¹ Y. Feng and W. Li contributed equally.

supported Pt or Pd catalysts, and then reduced by H₂ [18,19]. For instance, the Pb-promoted 5 wt%Pd/C catalyst yields pyruvic acid as high as 40% at 90 °C, pH = 8, and 60 g L⁻¹ catalyst [19]. Using Pb-, Bi-, and Sn-promoted 5 wt%Pt/C to catalyze the oxidation of PDO at semi-batch reaction gave a pyruvic acid yield up to 80% at 60 °C, pH = 8, 3.17×10^{-5} mol s⁻¹ O₂ flow rate, and 15 g L⁻¹ catalyst [18]. Since the conversion of PDO to pyruvic acid is a deeper oxidation process than to lactic acid [4], a relatively larger amount of catalyst is required. Considering the amount of noble metals used, the current transformation efficiency for pyruvic acid production is still less satisfactory. Pinxt et al. evaluate the effect of promoter (Pb, Bi, and Sn) on Pt/C catalyst for PDO oxidation, revealing that the Sn promoted Pt/C catalyst is the most effective for pyruvic acid production, of which the Sn is bound to the metallic Pt surface by reduction, coexisting in three chemical states, Sn⁰, Sn(II), and Sn(IV) [18]. From among of them, the Sn(IV) species could be more vital for enhancing the selective catalytic oxidation of PDO to pyruvic acid because the promoting effect of Sn could be due to the formation of a Sn–diol complex, where Sn is in the Sn(IV) state [18]. Nevertheless, it is still unclear whether the single Sn(IV) species can directly play as the promoter for improving the selective PDO oxidation to pyruvic acid or not. Thus, it is of great interest and significance to investigate the effect of Sn(IV) species as single promoter on the catalytic oxidation of PDO.

It is reported that the Sn(IV) centers can be incorporated into the framework of MCM-41 molecular sieve by the direct hydrothermal synthesis (DHS) method, resulting in active catalysts (Sn-MCM-41) for the Baeyer–Villiger oxidation with good conversion and high chemoselectivity due to the ordered mesoporous structure and high surface Sn (IV) dispersion [22]. Inspired by this, instead of introduction of promoters directly on the surface of noble metals, an alternative strategy of incorporating the promoters (Sn(IV) species) into the framework of support (MCM-41) is developed to construct effective catalyst for catalyzing the oxidation of PDO.

Hence, herein, a series of Sn(IV) species doping MCM-41 (designated as SnM) with different Si/Sn ratios were synthesized by the DHS method, and used to fabricate SnM supported Pd nanoparticles (Pd/SnM) catalysts by in situ reduction of Pd²⁺ anions on the SnM surface. For the Pd/SnM catalyst, the introduction of Sn(IV) species into MCM-41 can significantly enhance the selective PDO oxidation to pyruvic acid comparing with the non-Sn modified Pd/MCM catalyst, proving the positive promoting effect of Sn(IV) species. By tailoring the Sn doping amount, it can optimize the preferred catalyst for highly selective oxidation of PDO to pyruvic acid at mild reaction conditions. A possible reaction mechanism for the oxidation of PDO to pyruvic acid is proposed. This work provides an alternative effective catalyst for selective oxidation of PDO to pyruvic acid.

2. Experimental

2.1. Materials

The chemicals, cetyltrimethylammonium bromide (CTAB), tetraethyl orthosilicate (TEOS), ammonia (NH₃·H₂O), palladium chloride (PdCl₂), Tin (IV) chloride dehydrate (SnCl₄·5H₂O), sodium hydroxide (NaOH), 1,2-propanediol, lactic acid, pyruvic acid, acetic acid, and hydroxyacetone were of reagent grade and were purchased from Sinopharm Chemical Reagent Co., Ltd. China. Methanol was of chromatographic grade and was purchased from Sinopharm Chemical Reagent Co., Ltd. China. All chemicals were used as received without further purification.

2.2. Catalyst preparation

Nanosized Sn doping MCM-41 (SnM) samples with different mole ratio of Si/Sn were synthesized by the direct hydrothermal synthesis (DHS) method [23]. Typically, 2.77 g of CTAB was first dissolved in 120 g of deionized water. Then, 9.52 g of NH₃·H₂O was added in the solution under vigorous stirring for 10 min. Given amount of SnCl₄·5H₂O was mixed with 10.42 g of TEOS, and added dropwise to the above solution under vigorous stirring for 1 h until TEOS was completely dissolved. The gel mixture was then transferred into a Teflon-lined high-pressure autoclave and reacted at 110 °C for 48 h. The resulting solid product was recovered by filtration, washed with deionized water, and dried at 60 °C for 24 h. The as-synthesized samples were first calcined in air at 200 °C for 2 h with a heating rate of 5 °C min⁻¹, and then calcined at 550 °C for 6 h with a heating rate of 2 °C min⁻¹. By variation of the SnCl₄·5H₂O amount, SnM powder with mole ratios of Si/Sn = 50, 25, 12, and 6 were obtained, designated as SnM50, SnM25, SnM12, and SnM6, respectively.

SnM supported Pd nanoparticle catalysts with different compositions (designated as xPd/SnMy, where x is the weight percentage of Pd to support × 100%, and y is the mole ratio of Si/Sn) were prepared by the in situ chemical reduction method. Typically, 1 g of SnM12 powder was dispersed in 100 mL of deionized water at 60 °C under vigorous stirring. Given amount of PdCl₂ was dissolved in 1 M HCl and was then added into the above solution. The pH value of the mixed solution was adjusted to ca. 7 using 1 M NaOH solution. After being continuously stirred for 1 h, 0.25 g of ascorbic acid was added into the solution to reduce the Pd²⁺ ions. After reacting for 1 h, the resulting solid product was filtrated and washed by ethanol and deionized water for 3 times, respectively, and then dried at 100 °C overnight. By variation of the amount of PdCl₂, Pd/SnM catalysts with Pd amount of 1%, 2%, and 4% were prepared. As comparison, SnM50, SnM25, and SnM6 supported Pd nanoparticle catalysts with Pd mass ratio of 2% were prepared by the same method, as listed in Table 1.

Table 1
Summary of the characterization results for Pd/SnM catalysts.

Samples	Ratios of Si/Sn ^a (mol/mol)	Pd loadings ^a (wt%)	S _{BET} ^b (m ² g ⁻¹)	Pore volume ^b (cm ³ /g)	Pore diameter ^b (nm)	Particle size of Pd ^c (nm)	Pd dispersion ^d (%)	Percentage of metallic Pd ^e and oxidized Pd(II) (%)		Total basicities ^f (μmol _{CO2} g _{cat} ⁻¹)
								Pd ^e	Pd(II)	
2%Pd/MCM	∞	2.2	877	0.74	3.81	32.8	10.6	60.1	39.9	3.4
2%Pd/SnM50	67.3	2.2	706	0.64	3.80	21.4	13.6	57.7	42.3	8.5
2%Pd/SnM25	34.2	2.0	576	0.60	3.38	7.1	16.2	45.4	54.6	12.9
2%Pd/SnM12	17.3	1.9	503	0.51	3.16	4.0	17.3	43.9	56.1	15.2
2%Pd/SnM6	10.3	2.1	366	0.34	3.07	17.0	12.8	38.1	61.9	18.6

^a As calculated from the area of the metallic Pd species and oxidized Pd species in the XPS spectra of Pd 3d5/2.

^a As determined by ICP.

^b Calculated from N₂ adsorption-desorption.

^c As measured by TEM.

^d As determined by CO chemisorption at 25 °C.

^f The relative CO₂ desorption amount was obtained from CO₂-TPD.

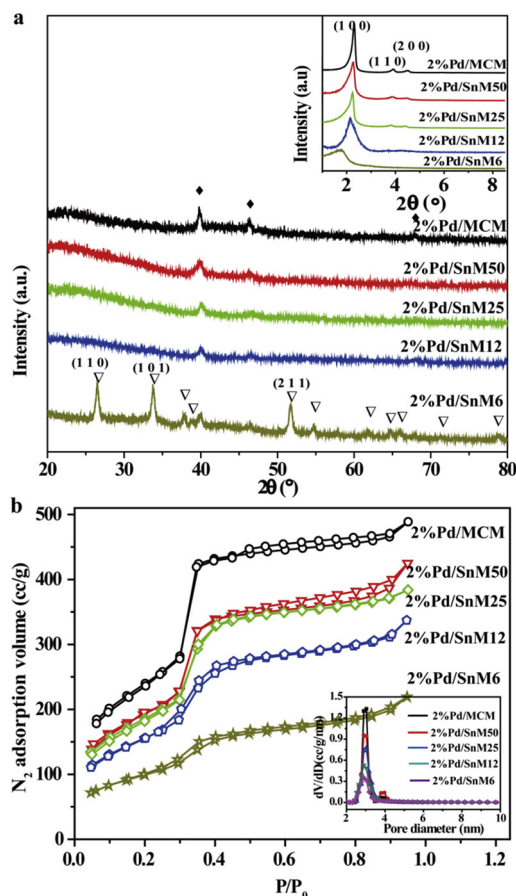


Fig. 1. XRD spectra of 2%Pd/SnM (a), and the inset is the corresponding low angle spectra of 2%Pd/SnM; and N_2 adsorption and desorption profiles of 2% Pd/SnM (b), and the inset is the corresponding pore size distributions based on DFT mode.

2.3. Characterization

Nitrogen adsorption-desorption isotherms were measured at -196°C by a NOVA 2000e physical adsorption apparatus. The specific surface areas (S_{BET}) and average pore size of the samples were determined by Brunauer–Emmett–Teller (BET) and Barrett–Joyner–Halenda (BJH) methods, respectively.

The powder X-ray diffraction (XRD) spectra of Pd/SnM samples were recorded on a diffractometer (D8 super speed Bruke-AEX Company, Germany) using Cu K α radiation ($\lambda = 1.54056 \text{ \AA}$) with Ni filter.

The UV–vis diffuse reflectance spectra (DRS) of the as-prepared SnM samples were obtained using a Shimadzu (Model UV-2550) spectrophotometer. The diffuse reflectance infrared Fourier transform spectroscopy (DRIFTS) was recorded using a Nicolet IS50 instrument equipped with a MCT detector and a KBr beam splitter. All spectra were collected in a nitrogen atmosphere at 200°C .

The NMR spectroscopic studies were carried out on Agilent 600 DD2 NMR spectrometer. The ^{29}Si and ^{119}Sn MAS NMR experiments were performed at a resonance frequency of 119.23 and 223.50 MHz, respectively. The ^{29}Si and ^{119}Sn NMR cross polarization (CP) spectra were recorded with a 4 mm NB probe at the spinning rates of 15 kHz and 8 kHz, respectively.

The scanning electron microscopy (SEM) was performed on a scanning electron microscope (JSM 7001 F) operated at an acceleration voltage of 10 kV to characterize the morphology of samples. The transmission electron microscopy (TEM) were performed on a transmission electron microscopy (Tecnai 12) operated at an acceleration

voltage of 120 KV. High resolution transmission electron microscopy (HRTEM) images and elemental mapping images were obtained on a microscopy (Tecnai G2 F30) operated at an acceleration voltage of 200 KV.

X-ray photoelectron spectra (XPS) of the catalysts were recorded on an XSAM800 spectrometer (Kratos Company) using Al K α radiation (1486.6 eV). The binding energies were calculated with respect to C1 s peak of contaminated carbon at 284.6 eV.

Temperature-programmed desorption of CO_2 (CO_2 -TPD) was carried out in a fixed-bed continuous flow microreactor at atmospheric pressure. 0.1 g of sample was first dried at 500°C for 2 h in helium. Then CO_2 was introduced to the sample at 100°C for 1 h. After purging with helium (30 mL min^{-1}) at 100°C for 0.5 h to remove the weakly adsorbed CO_2 , the TPD experiment was carried out at a linear heating rate of $15^\circ\text{C min}^{-1}$ from 100 to 950°C . In order to determine the amount of desorbed CO_2 from CO_2 desorption profiles, the areas under the curves were integrated by Gaussian deconvolution of the peaks and the amount of desorbed CO_2 was expressed as micromoles of CO_2 per gram of catalyst ($\mu\text{mol}_{\text{CO}_2} \text{ g}_{\text{cat}}^{-1}$).

The actual contents of Pd and Sn were determined by inductively coupled plasma (ICP) technique (VISTA-MPX). The dispersion of Pd was calculated on the basis of CO adsorption. Typically, 0.1 g of sample was first pretreated in hydrogen ($30 \text{ cm}^3 \text{ min}^{-1}$) at 150°C for 1 h and purged with helium ($30 \text{ cm}^3 \text{ min}^{-1}$) for 1 h at the same temperature, and then cooled to room temperature. CO pulses were injected from a calibrated on-line sampling valve. CO adsorption was assumed to be completed after three successive peaks at the same areas. A CO/Pd stoichiometry of 1 was used for calculations, and thus the Pd dispersion is calculated by the CO absorption amount (mol) divided by the Pd loading on catalyst (mol).

2.4. Catalysis test

The catalytic oxidation of 1,2-propanediol was performed in a 250 mL capacity stainless steel autoclave equipped with a magnetically driven impeller. The autoclave was charged with appointed amounts of 1,2-propanediol, water, sodium hydroxide, and catalyst. First, the autoclave was purged with O_2 for 10 min. Then the pressure was raised to the desired value. The reaction was carried out under stirring (800 rpm) at a given temperature for a certain time. After reaction, the autoclave was cooled to ambient temperature and depressurized. The concentration of remained 1,2-propanediol was analyzed on a gas phase chromatograph equipped with a PEG-20 M packed capillary column ($0.25 \text{ mm} \times 30 \text{ m}$) and FID by the internal standard method with n-butanol as the internal standard. The products were analyzed on a Agilent HPLC system equipped with a strong cation hydrogen exchange column (carboximix H-NP, $7.8 \text{ mm} \times 300 \text{ mm}$) and a UV detector ($\lambda = 210 \text{ nm}$) at 35°C . Before analysis, the reaction mixture was acidified with hydrochloric acid (12 M) to the pH value of 2–3. Sulphuric acid (5 mM) was used as a mobile phase with a flow rate of 0.6 mL min^{-1} . The concentrations of the products were analyzed by the external standard method.

3. Results and discussion

3.1. XRD analysis of Pd/SnM catalysts

The XRD patterns of Pd/SnM catalysts at low and high angles are given in Fig. 1a. As shown in the inset of Fig. 1a, three well-resolved diffraction peaks of $2\theta = 2.3, 3.9,$ and 4.5° , respectively, appearing at the low angle XRD pattern of 2%Pd/MCM are indexed to (1 0 0), (1 1 0) and (2 0 0) lattice planes of the mesoporous MCM-41 [24], indicating the catalyst maintains well mesoporous structure after the Pd nanoparticle immobilization. In the case of the low angle XRD patterns of 2% Pd/SnM, the diffraction peaks of 2%Pd/SnM50, 2%Pd/SnM25, and 2% Pd/SnM12 are similar to those of 2%Pd/MCM but the intensity slightly

decreases (especially for the diffraction peaks of (1 1 0) and (2 0 0) planes of 2%Pd/SnM12), and the shape becomes broader and shifted to low angle ($2\theta = 2.1^\circ$ for 2%Pd/SnM12), which can be attributed to that more Sn^{4+} isomorphously replace the Si^{4+} and incorporate into the framework of MCM-41 with decreasing the Si/Sn ratio [25]. The result indicates the 2%Pd/SnM12–50 catalysts well maintain the ordered hexagonal mesoporous framework. Further decreasing the Si/Sn ratio to 6, it is observed that the diffraction peak of (1 0 0) plane of 2%Pd/SnM6 becomes much broader and shifts to $2\theta = 1.7^\circ$, and the diffraction peaks of (1 1 0) and (2 0 0) planes disappear, indicating high Sn content (2%Pd/SnM6) could lead to the decrease in crystallinity of mesoporous molecular sieve.

The high angle patterns of 2%Pd/SnM12–50 are similar to that of 2%Pd/MCM and no crystalline SnO_2 phase is observed, indicating that Sn is highly dispersed in MCM-41. However, sharp diffractions of $2\theta = 26.6, 34.0$ and 51.7° corresponding to the (1 1 0), (1 0 1) and (2 1 1) planes of rutile phase SnO_2 (JCPDS 41–1445) appears for the 2%Pd/SnM6 [26], indicating the dispersion of Sn is poor in Pd/SnM(6), and a large number of Sn species existed in the form of SnO_2 in SnM(6). For all the samples, three diffraction peaks appearing at $2\theta = 40.0, 46.6$, and 68.0° can be indexed as the (1 1 1), (2 0 0), and (2 2 0) planes of the face-centered cubic (fcc) palladium (JCPDS 46–1043).

3.2. N_2 adsorption-desorption isotherm of Pd/SnM catalysts

The N_2 adsorption-desorption isotherms of 2%Pd/SnM are shown in Fig. 1b. With increasing Sn doping amount, the BET surface area and pore volume decrease from 877 to $366 \text{ m}^2 \text{ g}^{-1}$, and from 0.74 to $0.34 \text{ cm}^3 \text{ g}^{-1}$ (Table 1), respectively. It can be essentially due to more incorporation of Sn in MCM-41 [27]. The highly dispersed Pd nanoparticles occupying the space in mesoporous channels of the SnM can also cause the loss of micropores and BET surface area compared with siliceous MCM-41 [28]. The isotherm of 2%Pd/MCM shows a typical isotherm of mesoporous MCM-41. The typical type IV adsorption isotherms are observed for all 2%Pd/SnM, with the pore filling due to capillary condensation restricted to a narrow range of $P/P_0 = 0.25$ – 0.35 [24], indicating the 2%Pd/SnM maintain the mesoporous structure of MCM-41. Moreover, the pore size distributions of the 2%Pd/SnM6–50 (inset of Fig. 1b) are in a narrow range of 2–4 nm, indicative to the dominant mesoporous structure, consistent with the small angle of XRD characterization. The average pore sizes of the 2%Pd/SnM decrease with decreasing the Si/Sn ratios. It could be attributed to the smaller Pd nanoparticles owing higher distribution in situ growth on the surface of SnM [29]. The 2%Pd/SnM6 displays a significant decrease in the average pore size, probably due to the formation of SnO_2 crystallites, besides the Pd nanoparticles on the surface of SnM6, blocking the channels more seriously.

3.3. SEM, TEM, UV-vis, FTIR, and MAS NMR analysis of SnM samples

The SEM images of MCM-41 and SnM12 samples are shown in Figure S1. The MCM-41 and SnM12 exhibit similar morphology composed of spherical particulates with the average particle sizes of 62.2 and 76.3 nm, respectively, indicating the Sn(IV) incorporation does not significantly affect their morphologies but slightly increases the particle size. The TEM images of MCM-41 (Fig. S2a and b) show the well-ordered hexagonal array of uniform channels (Fig. S2a) and mesopores (Fig. S2b). Similar mesoporous structures are observed on the TEM images of SnM12 (Fig. S2c and d), and the two-dimensional hexagonal structure (P6mm) was confirmed, consistent with the XRD characterization [26]. The corresponding pore diameter was estimated to be ca. 3 nm, consistent of the N_2 adsorption and desorption analysis. The Sn (IV) species incorporated into the SnM samples can be further proved by the UV-vis DRS, FTIR, and MAS NMR characterizations, listed as below.

Figure S2e shows that the UV-vis DRS of SnM50, SnM12, and SnM6

reveal a strong absorption band in the region on 200–290 nm and a weak tail above 300 nm, assigning to charge transfer from O^{2-} to Sn^{4+} [30]. The strong absorption band can be deconvoluted into two peaks at ca. 220 and 242 nm, attributable to the Sn species in tetrahedral coordination and the polymeric Sn–O–Sn species in tetrahedral coordination, respectively [28,30]. The presence of tetrahedral coordination of Sn suggests that the Sn species are incorporated into the framework of MCM-41, in accordance with the report of Chaudhari et al [25]. Stronger relative intensity of this absorption band (220 nm) is observed for SnM12 comparing to SnM50, suggesting more Sn species are incorporated into the framework due to increasing the Sn doping amount. However, for SnM6 the absorption band at 242 nm is relatively stronger than that at 220 nm, indicating the presence of more hexacoordinated polymeric Sn–O–Sn-type species. Meanwhile, a new band at ca. 310 nm assigned to Sn^{4+} in octahedral coordination [28] is observed, demonstrating SnO_2 crystallites formed on SnM6 due to excess Sn doping, which is consistent with the XRD characterization.

The FTIR spectra of the MCM-41, SnM12, and SnM6 are shown in Figure S2f. The asymmetric Si–O–Si stretching at 1091 cm^{-1} and symmetric stretching at 814 cm^{-1} for MCM-41 are found to shift to lower wavenumbers for SnM12 and SnM6, probably due to the incorporation of Sn in the lattice [31]. The intensity of the typical absorption band at 970 cm^{-1} for the SnM12 is stronger than that for MCM-41, attributable to the incorporation of the heteroatom (Sn) into the framework [25]. Nevertheless, in the case of SnM6 this band is weak probably due to the formation of SnO_2 crystallites rather than the incorporation into the framework.

The ^{29}Si and ^{119}Sn MAS NMR spectra of SnM12 are shown in Figure S2g, in which the ^{29}Si MAS NMR spectrum of MCM-41 and ^{119}Sn MAS NMR spectrum of SnO_2 are used for reference, respectively. The broadness of the ^{29}Si signals can be attributed to the large distribution of the T–O–T angle [25,26]. The ^{29}Si spectrum of MCM-41 shows the bands at -103 and -113 ppm due to $\text{Si}(\text{OSi})_x(\text{OH})_{4-x}$ framework units where $x = 3(\text{Q}^3)$ and $x = 4(\text{Q}^4)$ respectively, while the ^{29}Si spectrum of SnM12 displays the bands at -103 and -110 ppm are due to the $\text{Si}(\text{OSi})_3(\text{OH})$ (Q^3) and the $\text{Si}(\text{OSi})$ environment (Q^4), respectively [26]. Moreover, a weak shoulder at around 116 ppm can be observed, attributable to the $\text{Si}(\text{1Sn})$ environment [26], indicative to the incorporation of Sn(IV) species into the framework. In the case of the ^{119}Sn MAS NMR spectra, though the natural abundance and the magnetogyric ratio of ^{119}Sn are higher than those of ^{29}Si the detection of Sn in stannosilicates is not easy due to the low concentration, long spin–lattice relaxation times, and, to some extent, the large chemical shift anisotropy (CSA) [25,26]. Nevertheless, an attempt has been made to record the ^{119}Sn MAS NMR spectrum of SnM12 sample. For the SnM12, an isotopic chemical shift of $\delta = -644 \text{ ppm}$ is observed. The isotopic chemical shift of octahedrally coordinated Sn in pure SnO_2 is of ca. $\delta = -607 \text{ ppm}$. Thus, the chemical shift value obtained for SnM12 can be attributed to the tetrahedral coordination of the Sn^{4+} ions [25,26].

3.4. TEM analysis of Pd/SnM catalysts

The TEM images of Pd/SnM with different Si/Sn ratios are shown in Fig. 2. The average particle sizes of Pd nanoparticles from TEM observation are listed in Table 1. For 2%Pd/MCM, relative larger spherical Pd nanoparticles with an average particle size of ca. 32.8 nm are anchored on the surface of MCM-41 support (Fig. 2a). For the 2%Pd/SnM12–50, as shown in Fig. 2b–d, the average Pd particle sizes decrease from ca. 21.4 nm to 4.0 nm with decreasing the Si/Sn ratios from 50 to 12, along with improving the distribution of the Pd nanoparticles on the supports. Nevertheless, the 2%Pd/SnM6 displays a relative larger Pd particle size, probably due to the presence of SnO_2 crystallites on the surface of SnM6 not beneficial for dispersing the Pd nanoparticles. As shown in Figure S3a, no significant aggregation of Pd nanoparticles is observed in the 4%Pd/SnM12 when the Pd loading is increased to 4.0%. The result indicates the SnM12 can well support and

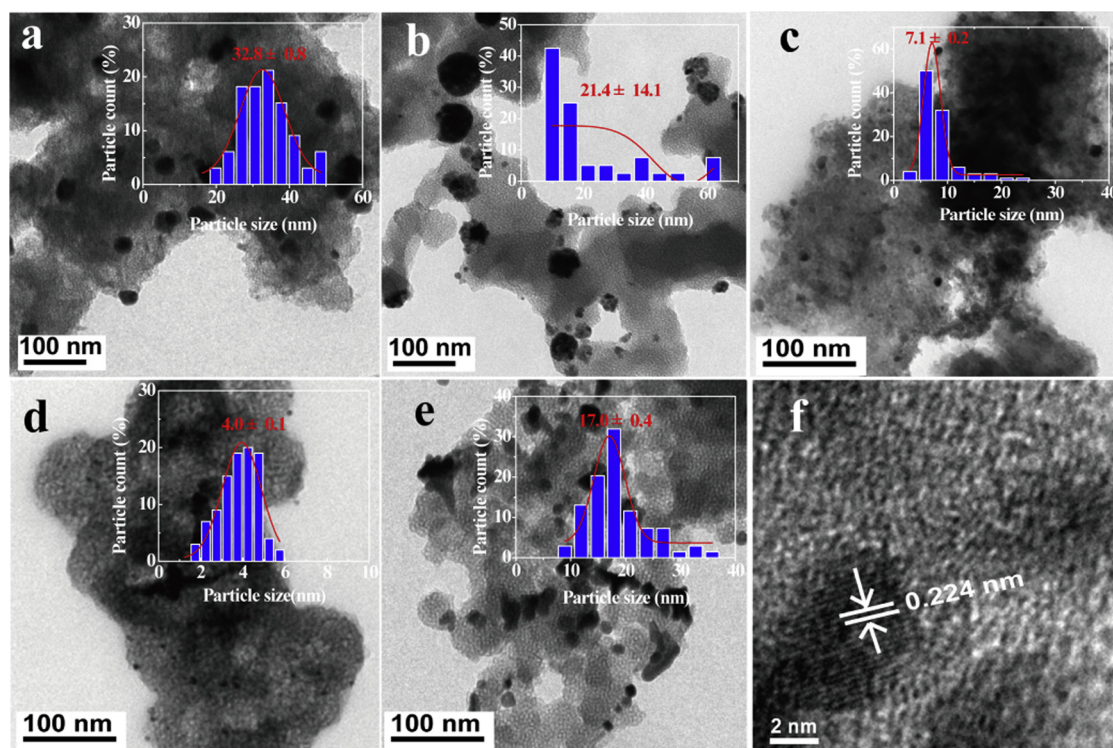


Fig. 2. TEM images of 2%Pd/SnM/MCM (a), 2%Pd/SnM50 (b), 2%Pd/SnM25 (c), 2%Pd/SnM/SnM12 (d) and 2%Pd/SnM6 (e), and HRTEM image of 2%Pd/SnM12 (f).

disperse Pd nanoparticles even at high Pd content. Fig. 2f shows the HRTEM image of 2%Pd/SnM12. The lattice spacing of ca. 0.224 nm can be assigned to the (1 1 1) plane of metallic Pd with a cubic phase. The Pd nanoparticles on 2%Pd/SnM12 catalyst are single crystalline.

Figures 3a–f are the TEM image and corresponding element mapping of 2%Pd/SnM12. The signals of Si and O (Fig. 3b and c) were

mainly detected in the selected region. It is noteworthy that the signals of Sn distributed homogeneously within the region (Fig. 3d), and the signals of Sn are much lower than those of Si, which can be ascribed to the relatively low amount of Sn (Si/Sn = 12/1) incorporated into the framework of MCM-41. The signals of Pd focuses on the separated particulates in the selected region (Fig. 3e), revealing the well dispersed

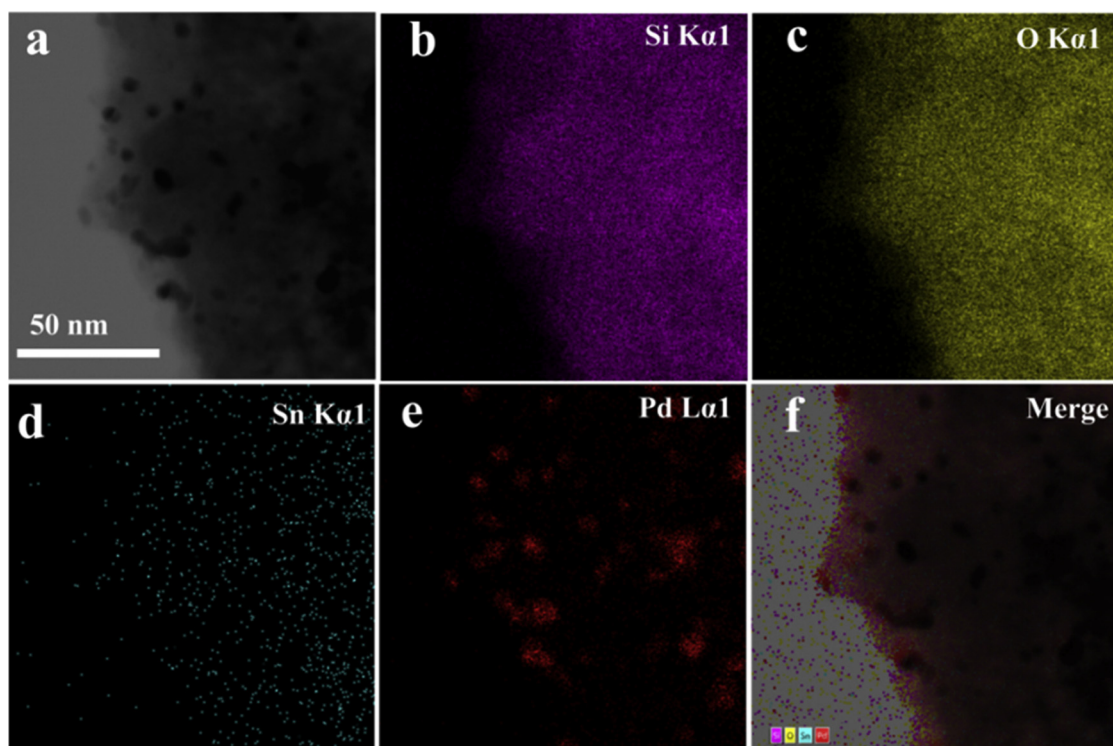


Fig. 3. TEM image (a) and corresponding element mapping of 2%Pd/SnM12, Si (b), O (c), Sn (d), Pd (e), and merge image (f).

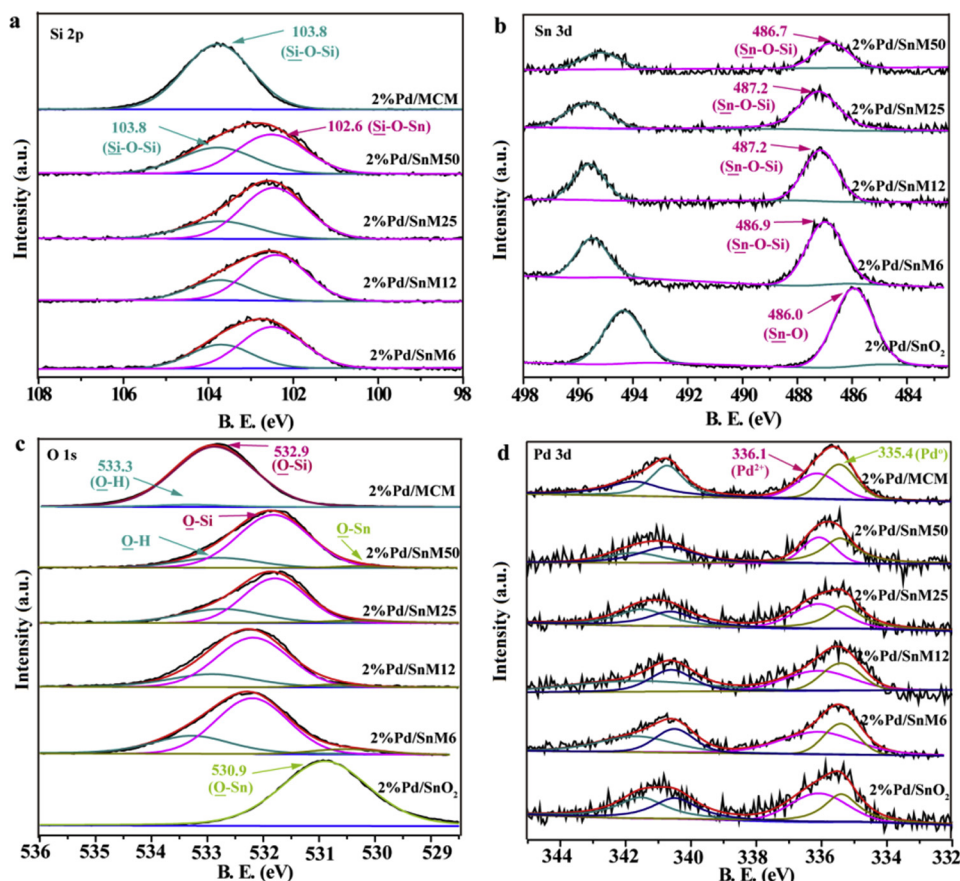


Fig. 4. XPS spectra of 2%Pd/MCM, 2%Pd/SnM6–50, and 2%Pd/SnO₂, (a) Si 2p, (b) Sn 3d, (c) O 1 s, and (d) Pd 3d spectra.

nano-size Pd particles on the surface of SnM12. The typical EDS spectrum taken from 2%Pd/SnM12 (Figure S4) further reveals the presence of respective elements of Pd, Sn, Si, and O. The atom ratios (At%) of Pd and Sn detected by EDS are higher than those of given amount, meaning more Pd and Sn expose on the surface of 2%Pd/SnM12 catalyst [32].

The Pd dispersions of 2%Pd/SnM based on the CO chemisorption (Table 1) display the catalyst owing smaller Pd particle size exhibits higher Pd dispersion, meaning more surface Pd atoms are exposed on the catalyst surfaces, which could be attributed to that smaller Pd particles have a better distribution on the support than the larger ones (TEM analysis) [33].

3.5. XPS analysis of Pd/SnM catalysts

The XPS spectra of Si, O, Sn, and Pd in 2%Pd/SnM catalysts are shown in Fig. 4, and 2%Pd/MCM and 2%Pd/SnO₂ catalysts are used as references. The Si 2p spectrum of 2%Pd/MCM in Fig. 4a shows single peak at 103.8 eV, assigning to the Si–O–Si of silica in MCM-41 [34]. The Si 2p spectra of 2%Pd/SnM can be deconvoluted into two obvious peaks at 103.8 and 102.6 eV, which could be assigned to the Si–O–Si and Si–O–Sn, respectively, attributable to the incorporation of Sn(IV) species into the framework. The ratios of peak area of 103.8 eV to 102.6 eV decreases with decreasing the Si/Sn ratios in 2%Pd/SnM catalysts, implying more Si–O–Sn are formed. Fig. 4b shows two typical doublets with the binding energies of ca. 494.3–495.2 eV and ca. 486.0–487.2 eV, which can be assigned to the 3d_{3/2} and 3d_{5/2} peaks of Sn⁴⁺, respectively [25]. As compared to the Sn 3d_{5/2} peak of Pd₂/SnO₂ (486.0 eV), the Sn 3d_{5/2} peaks of 2%Pd/SnM shifts to high binding energy (486.7–487.2 eV) [28], indicative to the formation of Sn–O–Si bonds in SnM support. Nevertheless, the shift of 2%Pd/SnM6 (486.9 eV) with highest Sn content is lower than that of 2%Pd/SnM12

(487.2 eV), which could be due to the relatively lower binding energy of SnO₂ crystallites formed on SnM6. In Fig. 4c, two deconvoluted peaks corresponding to O 1 s peak of 2%Pd/MCM are observed at 533.3 and 532.9 eV, assigning to $\overline{\text{O}}\text{--H}$ and $\overline{\text{O}}\text{--Si}$ bonds, respectively [26,35], while in 2%Pd/SnM6–50 three deconvoluted peaks are observed and can be assigned to $\overline{\text{O}}\text{--H}$ (533.3 eV), $\overline{\text{O}}\text{--Si}$ (532.3 eV), and $\overline{\text{O}}\text{--Sn}$ (530.9 eV) bonds, respectively [35,36]. The area ratio of $\overline{\text{O}}\text{--H}$ in 2%Pd/SnM catalysts increases with the increase in Sn doping amount, indicating more surface hydroxyl groups expose on the surface of SnM support. Larger area of the $\overline{\text{O}}\text{--Sn}$ peak at 530.9 eV is observed for 2%Pd/SnM6, indicating more $\overline{\text{O}}\text{--Sn}$ bonds present on SnM6 surfaces probably due to the formation of SnO₂ crystallites. As shown in Fig. 4d, the Pd 3d_{5/2} spectra of the samples can be deconvoluted into two obvious peaks at ca. 335.4 and 336.1 eV, assigned to the metallic Pd⁰ species [37], and oxidized Pd(II) species [38,39], respectively. Higher oxidized Pd(II) species content (Table 1) is observed for the 2%Pd/SnM than the 2%Pd/MCM, indicating there is stronger electron transfer from the Pd nanoparticles to the SnM than to the MCM-41. For the 2%Pd/SnM, an increasing abundance of Pd(II) owing to increasing Sn(IV) content (Table 1) suggests that, besides the anchorage of SnM through the functional group (eg. hydroxyl, epoxy) [40], an stronger interaction may also exist between the smaller Pd nanoparticles and surrounding Sn(IV) doping SiO₂ nanoparticles, which both probably contribute to the changes in the chemical state of surface Pd atoms [39,40]. The results indicate the Sn(IV) doping significantly affect the surface chemical states of Pd/SnM.

3.6. CO₂-TPD analysis of Pd/SnM catalysts

The surface basicity strength distribution of 2%Pd/SnM catalysts measured by CO₂-TPD is shown in Fig. 5, and the relative amount of

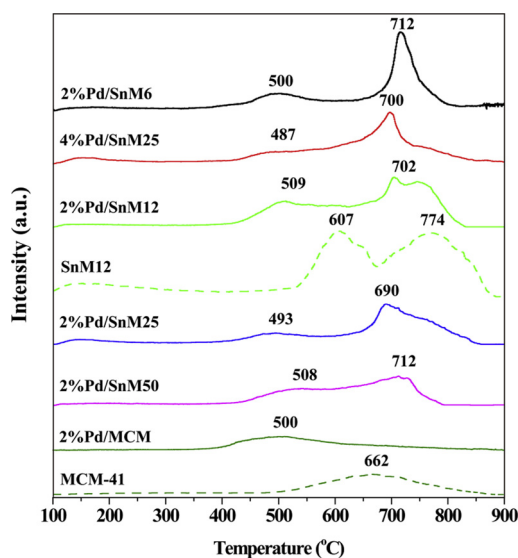


Fig. 5. CO₂-TPD profiles of SnM12, 2%Pd/MCM, and 2%Pd/SnM6–50.

surface basicity is listed in Table 1. No weak- (in range 100–200 °C) or medium- (in range 200–300 °C) strength basic sites are found in all the CO₂-TPD profiles. One weak peak at ca. 662 °C associated with strong-strength basic sites appears at the CO₂-TPD profile of MCM-41 due to the lack of surface basic sites of siliceous MCM-41 [24], while two strong peaks at ca. 607 and 774 °C, respectively are observed in the SnM12, indicative to two types of strong-strength basic sites on the surface of SnM12 [11]. It is found that the introduction of SnO₂ into BaCl₂-TiO₂ could significantly enhance the surface basicity of SnO₂-BaCl₂-TiO₂ [36]. Thus, the enhancement in the surface basicity of SnM compared to MCM-41 can be attributed to the Sn(IV) doping. Comparing with the CO₂-TPD profiles of pure MCM-41 and SnM12, the CO₂ desorption bands of 2%Pd/MCM and 2%Pd/SnM12 display lower intensity and lower desorption temperature, indicating the Pd nanoparticle loading can decrease their basicities. It may be due to the blocking effect of small-sized Pd nanoparticles. This can be more obvious when increasing the Pd loading on SnM12 from 2% to 4% (4%Pd/SnM12). For the 2%Pd/SnM catalysts, decreasing the Si/Sn ratio from 50 to 6 is beneficial for raising their basicity, probably due to more surface hydroxyl available on the SnM at high Sn content, as indicated by the XPS analysis (Fig. 3c).

3.7. Performances for catalytic PDO oxidation over Pd/SnM catalyst

No PDO conversion is observed when directly using the SnM12 as catalyst for catalyzing the PDO oxidation (Table 2). However, after loading with Pd nanoparticles, the 2%Pd/SnM12 displays high PDO conversion, along with the pyruvic acid (PA), lactic acid (LA), hydroxyl acetone (HA), and acetic acid (AA) as the detected products (Fig. 6, Table 2), implying the Pd nanoparticles can be the active sites. Fig. 6a shows prolonging the reaction time from 0 to 8 h, the PDO conversion significantly increases from 0% to 84.2%, but it can be only increased by 1.5% when further prolonging the reaction time to 10 h. Thus, herein, the PDO conversion at 8 h can be considered as the iso-conversion. Similar results can be observed with other catalysts for the PDO oxidation (Figure S5). For the product selectivities, prolonging the reaction time favors increasing the selectivities of pyruvic acid and acetic acid and slightly decreasing the selectivities of hydroxylacetone and lactic acid, revealing that the pyruvic acid and acetic acid can be the final products while the hydroxylacetone and lactic acid can be the intermediates. Fig. 6b shows the pH dependences of the PDO conversion and product selectivity. The pH of 8 can be optimal for the oxidation of 1,2-PDO to pyruvic acid over 2%Pd/SnM12 catalyst. Low pH

Table 2

Catalytic performance of Pd/SnM catalysts for PDO oxidation.

Samples	1,2-PDO conversions ^a (%)	Product selectivity (%)					TOF ^b (h ⁻¹)
		PA	LA	HA	AA	FA	
2%Pd/MCM	32.4	5.6	52.2	9	19.1	14.1	102
2%Pd/SnM50	51.7	67.5	8.3	8	16.2	0	98
2%Pd/SnM25	67.9	79.7	7.6	3.8	8.9	0	101
2%Pd/SnM12	84.2	84.3	5.3	3.7	6.7	0	132
2%Pd/SnM6	57.3	72.2	8.5	9.2	10.1	0	122
4%Pd/SnM12	90.2	87.3	3.6	3	6.1	0	95
1%Pd/SnM12	40.2	81.3	5.6	7	6.1	0	131
Pd ₂ /SnO ₂ ^c	27.5	64.8	14.5	5.8	14.9	0	70
Pd ₂ /Sn-C ^d	52.7	64.2	20.1	7.5	8.2	0	88
SnM12	0	0	0	0	0	0	–

^a Reaction conditions: 1,2-Propanediol concentration, 0.08 mol L⁻¹; pH = 8; Volume of solution, 40 mL; O₂ pressure, 1.0 MPa; Reaction temperature, 100 °C; Catalyst loading, 0.12 g; Reaction time, 8 h.

^b The initial turnover frequency (TOF) is calculated as the rate of PDO conversion at 1 h (Figure S5) referred to the number of surface Pd atoms which are calculated as the Pd loading on catalyst multiply by Pd dispersion.

^c The Pd₂/SnO₂ catalyst was prepared with SnO₂ as support, which was synthesized by precipitation method with SnCl₄ as the tin source and NH₃·H₂O as the precipitant.

^d The Pd₂/Sn-C catalyst was prepared by calcination of the SnCl₄ impregnated Pd₂/C catalyst at 400 °C without H₂ reduction, of which the Sn loading was similar to that of 2%Pd/SnM12 catalyst with the S_{BET} of higher than 800 m² g⁻¹.

(pH = 7) gives low PDO conversion and pyruvic acid selectivity since alkaline condition is crucial for the aqueous dehydrogenation and oxidation of polyol [7,15], while high pH (pH = 10) with more OH⁻ displays relative high lactic acid selectivity since it can facilitate the internal Cannizzaro reaction to form more lactic acid [7,10,12]. Fig. 6c and d show increasing the reaction temperature and the O₂ pressure favor higher PDO conversion but meanwhile lead to higher yield of acetic acid (a C2 product), probably due to increasing the C–C cleavage of C₃ products [4]. Fig. 6e shows the yield of pyruvic acid increases with decreasing the PDO concentration. The PDO conversion and pyruvic acid selectivity also depend on the amount of catalyst loading but high catalyst loading can easily lead to yielding more acetic acid (Fig. 6f).

The effect of the Sn(IV) species on the catalytic performance over the Pd/SnM catalyst was investigated at the optimized reaction conditions, at which all the catalytic reactions can almost reach the final PDO conversion (Fig. S5), as listed in Table 2. When using 2%Pd/MCM as the catalyst, five products including pyruvic acid, lactic acid, hydroxyl acetone, acetic acid, and formic acid (Table 2) are observed. The lactic acid is the dominant product with the PDO conversion of 32.4%. Different from the 2%Pd/MCM, the 2%Pd/SnM can produce four products but without the formic acid. Among them, the pyruvic acid is the dominant product. Moreover, higher PDO conversions are obtained. It demonstrates the Sn(IV) species in the Pd/SnM catalyst can effectively promote the selective catalytic oxidation of PDO to pyruvic acid, which can be ascribed to the special interaction between Sn(IV) species and PDO (Sn-diol complex) activating the PDO molecule [18], and the strong basicity enhancing the dehydrogenation [11]. For the 2%Pd/SnM12–50, decreasing the Si/Sn ratios from 50 to 12 can increase the PDO conversion and pyruvic acid selectivity from 51.7%–84.2% and from 67.5%–84.3% respectively, suggesting that high Sn(IV) doping amount is beneficial for improving the yield of pyruvic acid. However, in spite of the highest Sn content the 2%Pd/SnM6 displays much lower activity than the 2%Pd/SnM12. This may be due to the less ordered mesoporous structure and lower surface area of SnM6. Moreover, the presence SnO₂ crystallites on SnM6 could go against the enhancement in the catalytic activity because the single SnO₂ is found to be a less

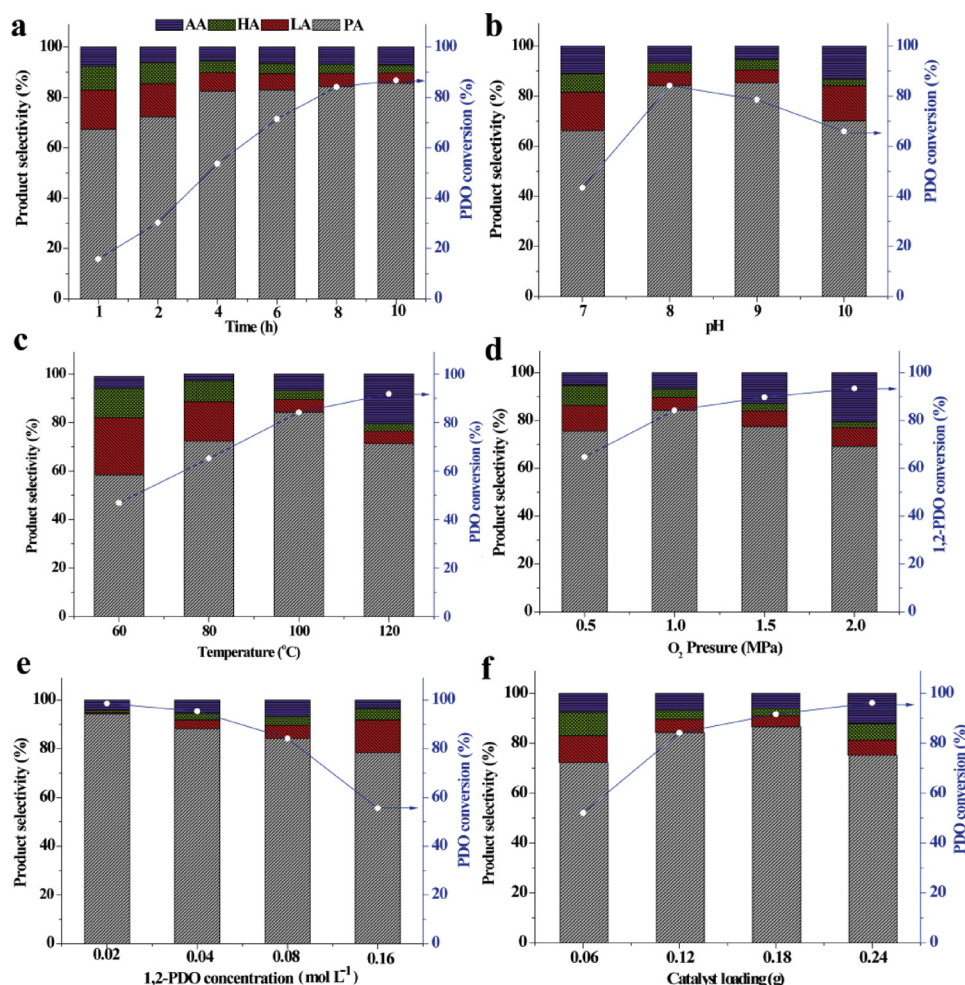


Fig. 6. The effects of reaction time (a), pH (b), temperature (c), O₂ pressure (d), PDO concentration (e), and catalyst loading (f) of 2%Pd/SnM12 on the catalytic PDO oxidation. The reaction conditions for (a): PDO concentration, 0.08 mol L⁻¹; pH = 8; volume of solution, 40 mL; O₂ pressure, 1.0 MPa; reaction temperature, 100 °C; catalyst loading, 0.12 g. The reaction conditions for (b–f) were similar to (a) but only change the corresponding parameter (pH, reaction temperature, O₂ pressure, PDO concentration, or catalyst loading) and keep the reaction time for 8 h.

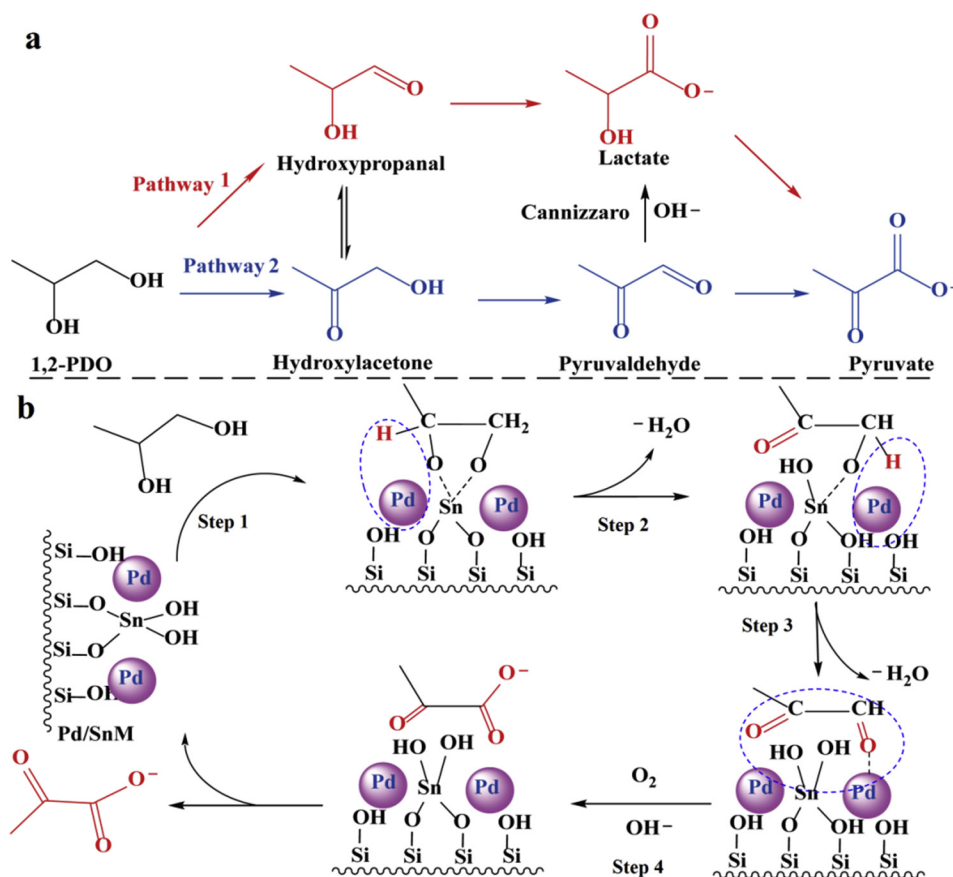
active support for the PDO oxidation (2%Pd/SnO₂, Table 2). Although cooperating with the active carbon (2%Pd/Sn-C) can be able to slightly improve the catalytic activity but still much lower than that of the 2%Pd/SnM12. Thus, it suggests that the Sn(IV) doping in MCM-41 is very vital for enhancing the selective catalytic PDO oxidation to pyruvic acid over the Pd/SnM catalyst.

The TEM characterization shows increasing the Sn(IV) content favors the formation of smaller Pd particles on the SnM support, which could also be responsible for the enhancement in the selective oxidation of PDO since smaller-sized Pd particles have more surface active Pd⁰ atoms due to the higher Pd dispersion (Table 1). As listed in Table 2, the PDO conversions and the pyruvic acid selectivities over the 2%Pd/SnM catalysts follow the order of 2%Pd/SnM12 (84.2%, 84.3%) > 2%Pd/SnM25 (67.9%, 79.7%) > 2%Pd/SnM6 (57.3%, 72.2%) > 2%Pd/SnM50 (51.7%, 67.5%), consistent with their Pd particle size order (Table 1). It demonstrates smaller-sized Pd particles favors higher yield of pyruvic acid. Nevertheless, in spite of the smallest Pd particles (4.0 nm), the catalytic activity (TOF) of 2%Pd/SnM12 is not apparently higher than the others (Table 2). This could be ascribed to the smaller-sized Pd particles having a larger ratio of oxidized Pd(II) species (Table 1) that might not be active sites for the PDO oxidation. For the 1–4%Pd/SnM12, increasing the Pd loading on SnM12 helps the increment of the PDO conversion due to more available active sites but slightly decreases the pyruvic acid selectivity.

Based on the above result, it can see the 2%Pd/SnM12 is the optimal

catalyst for the selective oxidation of PDO to pyruvic acid. Thus, it is significant to evaluate its recycling performance. As shown in Figure S6, after recycling for 4 times, the 2%Pd/SnM12 gives the PDO conversion of 82.7% with the pyruvic acid selectivity of 80.5%. The Pd weight percentage and the Si/Sn ratio in the spent 2%Pd/SnM12 are 1.67% and 18.4 (Table S1), respectively, after recycling for 4 times, indicating only small amount of Pd and Sn are leaked during the reaction as compared to those in the fresh catalyst. Moreover, the composition and the morphology of the used 2%Pd/SnM12 (Figure S7) are similar to those of the fresh catalyst. The results indicate the 2%Pd/SnM12 has good recycling performance.

Generally, as shown in Scheme 1a, the catalytic oxidation of PDO over supported noble metal catalysts can follow two reaction pathways 1 and 2 to form C₃ products [7,14,18,19]. Herein, the 2%Pd/SnM12 is used to catalyze the proposed intermediates of PDO oxidation to better understand the oxidation reaction network of PDO over Pd/SnM catalyst. The results are listed in Table 3. When the 2%Pd/SnM12 catalyzes the oxidation of PDO for 1 h, typical C₃ products from Scheme 1 are detected, including hydroxylacetone, lactic acid, and pyruvic acid. No pyruvaldehyde (PAH) or hydroxypropanal is observed since these two aldehydes are rather reactive in alkaline media [18]. The presence of byproduct acetic acid reveals the C–C cleavage occurs under these reaction conditions. It is expected that C–C cleavage will yield equimolar C₁ and C₂ products (C₃ = C₁ + C₂). Formic acid and carbonate are considered as the likely C₁ byproducts; however, no formic acid is observed



Scheme 1. The reaction network of PDO oxidation to lactate and pyruvate through Pathway 1 (P1) and Pathway 2 (P2) in alkaline solution (a), and proposed reaction route for the catalytic oxidation of PDO to pyruvate over Pd/SnM catalyst (b).

under our experimental conditions. Thus, carbonate could be the C₁ byproduct in this study although it has not been detected. The 2%Pd/MCM physically mixed with SnO₂ (2%Pd/MCM + SnO₂) can hardly enhance the selective PDO oxidation to lactic acid or pyruvic acid, indicating the Sn(IV) doping in the catalyst is vital for promoting the PDO oxidation to pyruvic acid. The oxidation of hydroxylacetone over 2%

Pd/SnM12 leads to high yield of pyruvic acid with low amounts of lactic acid and acetic acid at a completed conversion. No pyruvaldehyde, which is proposed as an oxidized intermediate for hydroxylacetone towards pyruvic acid [4,18,19], is shown, indicating it reacts relatively fast under the reaction conditions. Even using the support (SnM12 and SnO₂) as catalyst, it can be fast converted but with

Table 3

Catalytic oxidation of proposed intermediates formed in PDO oxidation process over 2%Pd/SnM12 or 2%Pd/MCM catalysts.

Intermediate	Catalyst	Conversion ^a	Product selectivity (%)				
			PA	LA	HA	AA	FA
PDO	2%Pd/SnM12	15.4	67.4	15.5	9.6	7.5	–
	2%Pd/MCM	7.5	5.2	58.7	11.5	14.4	10.2
HA	2%Pd/MCM + SnO ₂ ^b	10.2	4.1	35.2	9.5	41.2	10
	2%Pd/SnM12	99.9	81.1	12.6	–	6.3	0
PAH	2%Pd/MCM	99.9	16.8	63.2	–	12.7	7.3
	2%Pd/SnM12	99.6	93.5	0.7	–	5.8	0
	2%Pd/MCM	98.7	0	53.4	–	32.4	14.2
	2%Pd/MCM + SnO ₂	97.3	7.5	38.6	–	38.6	15.2
	SnO ₂	95.4	11.2	44.5	–	33.2	11.1
	SnM(12)	94.5	22.4	35.2	–	35.8	16.6
LA	2%Pd/SnM12	85.3	95.0	–	–	5.0	–
	2%Pd/MCM	4.4	56.4	–	–	30.6	14.0
PA	2%Pd/SnM12	3.6	–	–	–	100	–
	2%Pd/MCM	0	–	–	–	–	–
AA	2%Pd/SnM12	0	–	–	–	–	–
	2%Pd/MCM	0	–	–	–	–	–
FA	2%Pd/SnM12	0	–	–	–	–	–
	2%Pd/MCM	0	–	–	–	–	–

^a Reaction conditions: Substrate concentration, 0.08 mol L⁻¹; pH = 8; Volume of solution, 40 mL; O₂ pressure, 1.0 MPa; Reaction temperature, 100 °C; Catalyst loading, 0.12 g; Reaction time, 1 h.

^b The physical mixture of SnO₂ and 2%Pd/MCM, in which the SnO₂ loading is similar to that in 2%Pd/SnM12.

poor C3 product selectivity due to its instability under alkaline condition and relatively high reaction temperature [14]. The formation of lactic acid from hydroxylacetone suggests the side reaction of pyruvaldehyde undergoing an internal Cannizzaro reaction occurs. The observation of acetic acid points to the C–C cleavage, probably from the cleavage of pyruvaldehyde or pyruvic acid because the oxidation of the two substrates over 2%Pd/SnM12 produces acetic acid (Table 2). The oxidation of pyruvaldehyde and lactic acid over 2%Pd/SnM12 gives high pyruvic acid yield, but the oxidation of acetic acid and formic acid over the 2%Pd/SnM12 can hardly proceed. The relative stability of formic acid supports the hypothesis that the carbonate instead of formic acid is the C₁ product of C–C cleavage during the PDO oxidation catalyzed by 2%Pd/SnM12 [4,18].

During the PDO oxidation catalyzed by 2%Pd/SnM12, hydroxylacetone is observed, and the obtained pyruvic acid selectivity is similar to that in the direct oxidation of hydroxylacetone over 2%Pd/SnM12. Thus, it is proposed the selective catalytic oxidation of PDO to pyruvic acid over Pd/SnM catalyst could predominately follow the Pathway 2, as shown in Scheme 1b. The high activity of Pd/SnM could be related to the regioselectivity because the Sn(IV) species could interact with the PDO molecules to form Sn-diol complex (step 1, Scheme 1b) [18], promoting the dissociation of C–H bond to hydroxylacetone over metallic Pd nanoparticles (step 2, Scheme 1b) [8]. The hydroxylacetone is subsequently oxidized to pyruvaldehyde (step 3, Scheme 1b), and finally to pyruvic acid over metallic Pd nanoparticles (step 4, Scheme 1b). The Pathway 1 could proceed simultaneously but not predominately since the lactic acid is observed and it can be directly oxidized to pyruvic acid (Table 3).

4. Conclusions

Herein, a series of Pd/SnM catalysts are prepared by in situ reduction of Pd²⁺ ions on the surface of SnM synthesized by the DHS method. The Pd/SnM catalysts maintain good mesoporous structure and the Sn(IV) species are well incorporated into the framework of MCM-41. Increasing the Sn doping amount is beneficial for forming smaller Pd particles and improving the surface basicity of the catalysts, but excess Sn(IV) doping can lead to the formation of SnO₂ crystallites on SnM. During the catalytic PDO oxidation over Pd/SnM catalysts, the Pd nanoparticles act as the active site and the Sn(IV) species as the promoter. Both the Sn(IV) doping and the mesoporous structure of the Pd/SnM catalyst are responsible for the enhanced catalytic activity in the selective PDO oxidation to pyruvic acid. The 2%Pd/SnM12 owing proper Sn(IV) doping amount and the smallest Pd nanoparticles displays the highest catalytic activity in PDO oxidation. This work provides an alternative and effective route for the selective oxidation of PDO to pyruvic acid.

Acknowledgements

This work was financially supported by the National Natural Science Foundation of China (No. 21606112), China Postdoctoral Foundation Committee (No. 2016M600372), Natural Science Foundation of Jiangsu Province (No. BK20160503), Post Doctoral Fund of Jiangsu Province (No. 1601022 A), Natural Science Fund for Colleges and Universities in Jiangsu Province (No. 17KJB180001), the Six Talent Peaks Project of Jiangsu Province (No. 2016-XCL-016), Programs of Senior Talent Foundation of Jiangsu University (No. 15JDG137), and Youth Talent Cultivation Plan of Jiangsu University.

Appendix A. Supplementary data

Supplementary material related to this article can be found, in the

online version, at doi:<https://doi.org/10.1016/j.apcatb.2019.04.051>.

References

- [1] M. Pagliaro, R. Ciriminna, H. Kimura, M. Rossi, C. Della Pina, *Angew. Chemie Int. Ed.* 46 (2007) 4434–4440.
- [2] A. Marinas, P. Bruijninx, J. Ftouni, F.J. Urbano, C. Pinel, *Catal. Today* 239 (2015) 31–37.
- [3] Y. Feng, H. Yin, A. Wang, D. Gao, X. Zhu, L. Shen, M. Meng, *Appl. Catal. A Gen.* 482 (2014) 49–60.
- [4] D.J. Chadderton, L. Xin, J. Qi, B. Brady, J.A. Miller, K. Sun, M.J. Janik, W. Li, *ACS Catal.* 5 (2015) 6926–6936.
- [5] Y. Ryabenkova, Q. He, P.J. Miedziak, N.F. Dummer, S.H. Taylor, A.F. Carley, D.J. Morgan, N. Dimitratos, D.J. Willock, D. Bethell, D.W. Knight, D. Chadwick, C.J. Kiely, G.J. Hutchings, *Catal. Today* 203 (2013) 139–145.
- [6] E. Redina, A. Greish, R. Novikov, A. Strelkova, O. Kirichenko, O. Tkachenko, G. Kapustin, I. Sinev, L. Kustov, *Appl. Catal. A Gen.* 491 (2015) 170–183.
- [7] N. Dimitratos, J.A. Lopez-Sanchez, S. Meenakshisundaram, J.M. Anthonykutti, G. Brett, A.F. Carley, S.H. Taylor, D.W. Knight, G.J. Hutchings, *Green Chem.* 11 (2009) 1209–1216.
- [8] M.B. Griffin, A.A. Rodriguez, M.M. Montemore, J.R. Monnier, C.T. Williams, J.W. Medlin, *J. Catal.* 307 (2013) 111–120.
- [9] P.G.N. Mertens, M. Bulut, L.E.M. Gevers, I.F.J. Vankelecom, P.A. Jacobs, D.E.D. Vos, *Catal. Lett.* 102 (2005) 57–61.
- [10] Y. Ryabenkova, P.J. Miedziak, N.F. Dummer, S.H. Taylor, N. Dimitratos, D.J. Willock, D. Bethell, D.W. Knight, G.J. Hutchings, *Top. Catal.* 55 (2012) 1283–1288.
- [11] Y. Feng, H. Yin, D. Gao, A. Wang, L. Shen, M. Meng, *J. Catal.* 316 (2014) 67–77.
- [12] H. Ma, X. Nie, J. Cai, C. Chen, J. Gao, H. Miao, J. Xu, *Sci. China Chem.* 53 (2010) 1497–1501.
- [13] C. D'Agostino, Y. Ryabenkova, P.J. Miedziak, S.H. Taylor, G.J. Hutchings, L.F. Gladden, M.D. Mantle, *Catal. Sci. Technol.* 4 (2014) 1313–1322.
- [14] Y. Feng, H. Yin, A. Wang, W. Xue, *J. Catal.* 326 (2015) 26–37.
- [15] Y. Feng, W. Xue, H. Yin, M. Meng, A. Wang, S. Liu, *RSC Adv.* 5 (2015) 106918–106929.
- [16] W. Xue, Y. Feng, H. Yin, S. Liu, A. Wang, L. Shen, *J. Nanosci. Nanotechnol.* 16 (2016) 9621–9633.
- [17] D. Tongsakul, S. Nishimura, K. Ebitani, *J. Phys. Chem. C* 118 (2014) 11723–11730.
- [18] H.H.C.M. Pinxt, B.F.M. Kuster, G.B. Marin, *Appl. Catal. A Gen.* 191 (2000) 45–54.
- [19] T. Tsujino, S. Ohgashi, S. Sugiyama, K. Kawashiro, H. Hayashi, *J. Mol. Catal.* 71 (1992) 25–35.
- [20] D. Pal, A. Keshav, B. Mazumdar, A. Kumar, H. Uslu, *J. Inst. Eng. India Ser. E* 98 (2017) 165–175.
- [21] C. Zhang, T. Wang, Y. Ding, *Appl. Catal. A Gen.* 533 (2017) 59–65.
- [22] A. Corma, M.A. Navarro, M. Renz, *J. Catal.* 219 (2003) 242–246.
- [23] M. Grün, K.K. Unger, A. Matsumoto, K. Tsutsumi, *Micropor. Microporous Mesoporous Mater.* 27 (1999) 207–216.
- [24] S.C. Shen, X. Chen, S. Kawi, *Langmuir* 20 (2004) 9130–9137.
- [25] K. Chaudhari, T.K. Das, P.R. Rajmohan, K. Lazar, S. Sivasanker, A.J. Chandwadkar, *J. Catal.* 183 (1999) 281–291.
- [26] P. Shah, A.V. Ramaswamy, K. Lazar, V. Ramaswamy, *Appl. Catal. A Gen.* 273 (2004) 239–248.
- [27] L. G. Z. L. Y. X. W. J. L. H. J. Inorg. Mater. 25 (2010) 1041–1046.
- [28] G. Luo, S. Yan, M. Qiao, K. Fan, *Appl. Catal. A Gen.* 332 (2007) 79–88.
- [29] Á. Mastalir, B. Rác, Z. Király, Á. Molnár, *J. Mol. Catal. A Chem.* 264 (2007) 170–178.
- [30] S. Samanta, N.K. Mal, A. Manna, A. Bhaumik, *Appl. Catal. A Gen.* 273 (2004) 157–161.
- [31] N. Kishor Mal, V. Ramaswamy, S. Ganapathy, A.V. Ramaswamy, *Appl. Catal. A Gen.* 125 (1995) 233–245.
- [32] J. Zhang, Y. Feng, J. Mi, Y. Shen, Z. Tu, L. Liu, *J. Hazard. Mater.* 342 (2018) 121–130.
- [33] A.N. Ardila, M.A. Sánchez-Castillo, T.A. Zepeda, A.L. Villa, G.A. Fuentes, *Appl. Catal. B Environ.* 219 (2017) 658–671.
- [34] B.M. Reddy, I. Ganesh, E.P. Reddy, *J. Phys. Chem. B* 101 (1997) 1769–1774.
- [35] E.P. Reddy, L. Davydov, P.G. Smirniotis, *J. Phys. Chem. B* 106 (2002) 3394–3401.
- [36] Z. Wang, G. Zou, X. Luo, H. Liu, R. Gao, L. Chou, X. Wang, *J. Nat. Gas Chem.* 21 (2012) 49–55.
- [37] C. Sener, T. Dogu, G. Dogu, *Micropor. Microporous Mesoporous Mater.* 94 (2006) 89–98.
- [38] R. Nie, M. Miao, W. Du, J. Shi, Y. Liu, Z. Hou, *Appl. Catal. B Environ.* 180 (2016) 607–613.
- [39] R. Nie, J. Shi, W. Du, Z. Hou, *Appl. Catal. A Gen.* 473 (2014) 1–6.
- [40] R. Kou, Y. Shao, D. Mei, Z. Nie, D. Wang, C. Wang, V.V. Viswanathan, S. Park, I.A. Aksay, Y. Lin, Y. Wang, J. Liu, *J. Am. Chem. Soc.* 133 (2011) 2541–2547.